

Orbital polarization in strained LaNiO₃: Structural distortions and correlation effectsOleg E. Peil,^{1,2,*} Michel Ferrero,² and Antoine Georges^{1,2,3}¹*Département de Physique de la Matière Condensée, University of Geneva, 24 Quai Ernest-Ansermet, 1211 Genève 4, Switzerland*²*Centre de Physique Théorique, Ecole Polytechnique, CNRS, 91128 Palaiseau Cedex, France*³*Collège de France, 11 place Marcelin Berthelot, 75005 Paris, France*

(Received 19 April 2014; revised manuscript received 20 June 2014; published 23 July 2014)

Transition-metal heterostructures offer the fascinating possibility of controlling orbital degrees of freedom via strain. Here, we investigate theoretically the degree of orbital polarization that can be induced by epitaxial strain in LaNiO₃ films. Using combined electronic structure and dynamical mean-field theory methods we take into account both structural distortions and electron correlations and discuss their relative influence. We confirm that Hund's rule coupling tends to decrease the polarization and point out that this applies to both the $d^8\bar{L}$ and d^7 local configurations of the Ni ions. Our calculations are in good agreement with recent experiments, which revealed sizable orbital polarization under tensile strain. We discuss why full orbital polarization is hard to achieve in this specific system and emphasize the general limitations that must be overcome to achieve this goal.

DOI: [10.1103/PhysRevB.90.045128](https://doi.org/10.1103/PhysRevB.90.045128)

PACS number(s): 71.27.+a, 73.90.+f, 71.20.-b

I. INTRODUCTION

Ultrathin films and heterostructures of transition-metal oxides (TMOs) have attracted considerable interest in the past decade. Recent advances in TMO heterostructure and strain engineering have provided increased control of the electronic properties of TMOs. Furthermore, these structures exhibit novel behavior not found in their bulk counterparts [1–6].

The family of rare-earth nickelates [7,8], RNiO₃, has attracted particular attention in this context. Indeed, this class of materials has a rich phase diagram displaying a metal-to-paramagnetic-insulator, as well as a metal-to-magnetic-insulator transitions. These transitions are affected by the structural distortions depending, in turn, on the radius of the rare-earth ion. This interplay between structural and electronic properties makes this class of materials particularly suitable for heterostructure and strain engineering.

In this paper, we focus on LaNiO₃ (LNO). In bulk equilibrium form, this material is an exception among the RNiO₃ family since it remains a paramagnetic metal down to the lowest temperatures [9,10]. This metal has a rather high degree of electronic correlations, however, as signaled by the enhancement of the effective mass and susceptibility as compared to band values, as well as the sizable T^2 coefficient of the resistivity [10–13]. One may thus expect that this material can be rather easily tuned to become an insulator. Indeed, ultrathin LNO films were shown to become insulating under either dimensionality control [6,14,15] or epitaxial strain [16,17]. It was also demonstrated that both strain and dimensional confinement can drive an LNO film towards a spin-density-wave state, which is similar to what is observed in the insulating phase of other nickelates [18]. This makes LaNiO₃ a very suitable system for materials design by strain engineering and heterostructuring.

In a pioneering article, Chaloupka and Khaliullin [19] proposed that strained heterostructures of LNO could be used to engineer a material having an electronic structure consisting of a single band crossing the Fermi level. In view

of the strong electronic correlations in the Ni d shell, the low-energy effective model describing such a material might thus be quite analogous to the one appropriate for cuprates, hence suggesting a favorable situation for strong superexchange and possible high- T_c superconductivity. Indeed, the low-energy electronic structure at the Fermi level of bulk LaNiO₃ is primarily determined by the Ni³⁺ degenerate e_g states, which form a two-sheet Fermi surface [12,20]. One of the major effects of epitaxial strain or heterostructuring is the degeneracy lifting of the e_g states, resulting in orbital polarization (OP) of the electronic structure. The key question is whether conditions can be found such that this OP is large and the quasi-two-dimensional $d_{x^2-y^2}$ band is a dominantly occupied one with proper filling. This issue was previously investigated by Hansmann *et al.* [21,22] and Han *et al.* [23], for LaNiO₃/LaAlO₃ heterostructures, and proposals for achieving high OP by using other LNO-based heterostructures [24–27] or chemical control by other counterions [28,29] were made.

From a theoretical standpoint, the degree of orbital polarization has been a subject of controversy, mainly due to the need for a proper treatment of both strong correlation effects in the Ni d shell and of the strong hybridization effects with oxygen ligands [30,31]. In the work of Hansmann *et al.* [21,22], a low-energy description involving only the two e_g -like bands occupied by a single electron was considered (corresponding to the nominal d^7 occupancy of the Ni d shell). It was concluded there that correlation effects may lead to a considerable enhancement of the OP, mostly due to the effect of the on-site Coulomb repulsion U , as emphasized in previous model studies [32]. This conclusion was challenged by Han *et al.* [23], who pointed out that the joint effect of the Hund's rule coupling and of the strong hybridization with the ligand (associated with the relevance of the $d^8\bar{L}$ configuration) acts to reduce the OP, possibly down to a lower value than the one expected from band-structure calculations neglecting strong correlation effects. These issues were also considered at the model level in Ref. [33].

On the experimental side, x-ray absorption (XAS) and x-ray linear dichroism (XLD) spectroscopy, combined with resonant reflectivity, were recently performed [34] for a series of LNO heterostructures under a wide range of strains

*oleg.peil@gmail.com

from -2.3% to $+3.2\%$. These data clearly revealed that an orbital polarization $P = (n_{x^2-y^2} - n_{z^2}) / (n_{x^2-y^2} + n_{z^2})$ as high as 20–25% is achieved under tensile strain, with an essentially linear dependence of the polarization on strain. Note however that the results of another experimental investigation on thin films were interpreted as the occurrence of an octahedral breathing-mode distortion under tensile strain with negligible orbital polarization [35,36].

In this work, we investigate how strain affects the orbital degrees of freedom in LaNiO_3 epitaxial films. We take into account both the effect of strain-induced structural distortions and electronic correlations using many-body electronic structure methods. The calculated values of the orbital polarization as a function of strain are in good agreement with the experimental results of Ref. [34]. We also find that, for realistic values of interaction parameters, correlation effects associated with the Hund's rule coupling reduce the strain-induced polarization as compared to the value obtained from band-structure calculations, in agreement with the conclusions of previous works [23].

This paper is organized as follows. To begin with, we consider the effects of strain on the crystal structure of LaNiO_3 in Sec. II. Then we discuss the strain-induced orbital polarization, first from a band-structure standpoint (Sec. III) and then including electronic correlation effects in Sec. IV. Finally, we compare our theoretical calculations to experimental results and discuss in some details interpretations of the latter in Sec. V. Readers mostly interested in the final results may jump to this last section and, in particular, to Figs. 11 and 12. Also, some additional details can be found in Appendices A and B.

II. EFFECTS OF STRAIN ON THE STRUCTURE OF LaNiO_3

Most of the rare-earth (RE) nickelates possess a perovskite ABO_3 structure with various distortions depending on the temperature and composition [7,8]. In particular, the difference in ionic radii and the mismatch of the B-O and A-O equilibrium bond lengths d_{XO} result in octahedral tilts whose magnitude can be related to the tolerance ratio, $t = d_{AO}/d_{BO}\sqrt{2}$, quantifying the deviation of the bond-length ratio from the one of the ideal perovskite structure. The octahedral tilts lead to the decrease of Ni-O-Ni bond angles and the reduction of the $\text{Ni}d\text{-O}p$ hybridization, which, in turn, has a significant impact on the electronic structure. This effect is manifested in a direct dependence of the temperature of the metal-insulator transition (MIT) on t , with smaller t leading to higher critical temperatures [37]. Bulk LaNiO_3 , having the largest value of t , is the only compound in the family of RE nickelates that remains metallic and does not undergo a transition down to lowest temperatures.

Bulk LaNiO_3 has a perovskite structure with a rhombohedral distortion of the unit cell and the corresponding space group is $R\bar{3}c$ [38]. The rhombohedral distortion is induced by rotations of Ni-O octahedra with a rotation pattern of type $a^-a^-a^-$ (in Glazer notation [39,40]), which means that rotations around all three axes are anti-phase (the direction of the rotation around an axis is alternating along the given axis). This is in contrast to other nickelates having rotation pattern $a^-a^-c^+$ (GdFeO_3 type), i.e., with rotations around the a and

b axes being antiphase and the rotation around the c axis in phase.

The aim of this section is to determine how strain affects the structure of LaNiO_3 , as compared to the unstrained bulk.

A. Setup and method

We consider a layer of LaNiO_3 on a cubic or tetragonal substrate with a square in-plane face of the pseudo-cubic cell (as in STO or LSAT substrates).¹ A mismatch of the equilibrium lattice parameter between LNO and the substrate causes the LNO layer to be subject to biaxial strain in the ab plane. In nickelate films the strain can be sustained within rather thick films up to 20–50 atomic layers (depending on strain) [15], and we can thus neglect film-substrate interfacial as well as surface effects. The effect of the strain reduces then to a geometrical constraint on the bottom in-plane face of the pseudocubic cell of LNO.² Hence, a sufficiently thick film can be modeled by a bulklike geometry in which the in-plane lattice parameters (as well as the angle between the in-plane vectors) are fixed to those of the substrate and all other degrees of freedom are allowed to relax.

To identify the crystal structure of a strained film we perform structure optimization within generalized gradient approximation (GGA) [41] using the projected-augmented waves (PAW) method [42] as implemented in the Vienna *ab initio* simulation package (VASP) [43–45]. The integration over the Brillouin zone is done using a k mesh with $11 \times 11 \times 11$ points and the plane-wave cutoff is $E_{\text{cut}} = 600$ eV. Structure relaxation is considered to be converged when the forces are smaller than 10^{-3} eV/Å.

To simulate the LNO layer we set up a base-centered monoclinic unit cell (space group $C2/c$) oriented in such a way that Ni positions match those of B-ions of a [001]-oriented ABO_3 cubic substrate. This crystal space group is determined by the pattern of octahedral rotations (see Ref. [39]) and epitaxial constraints and was experimentally found in LNO/LAO and LNO/STO films [46]. The in-plane parameters of the pseudocubic cell, $a_p = b_p$, are fixed to that of the substrate, which determines the strain $\epsilon_{xx} \equiv a_p/a_{p,\text{eq}} - 1$, where $a_{p,\text{eq}}$ is the pseudocubic lattice parameter of bulk LNO ($a_{p,\text{eq}} = 3.863$ as obtained within GGA). All other degrees of freedom, such as the out-of-plane lattice vector, oxygen, and cation positions, are allowed to relax.

It is also instructive to compare the case of a relaxed monoclinic unit cell with the situation in which the system is constrained to remain tetragonal with no octahedral rotations (relaxing only c/a). Indeed, this reveals the role of the rotations and unit cell monoclinic distortion in the structural response to strain. In the following, we shall refer to the monoclinic and tetragonally constrained cases as distorted and tetragonal, respectively.

¹For such substrates all four possible orientations of the LNO trigonal rotation axis with respect to the substrate plane are equivalent [46].

²It is worth noting that since bulk LNO has a rhombohedrally distorted unit cell, a tetragonal substrate exerts a small *axial* strain (along a or b axis) on the film even when the biaxial strain is zero (as defined from the ratio of the lattice constants).

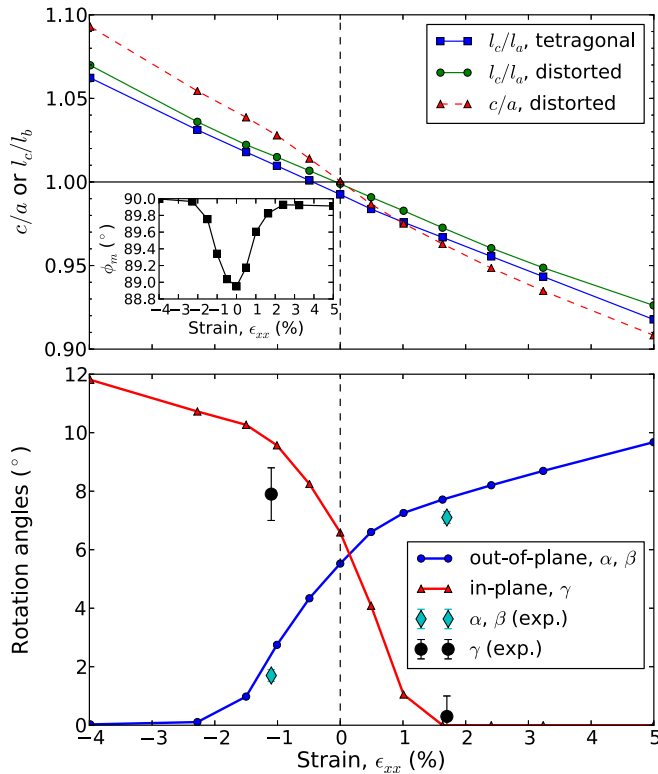


FIG. 1. (Color online) Top: Bond-length ratio, l_c/l_a , for the distorted (solid green) and tetragonal (solid blue) structures under strain. The broken line displays the c/a ratio for the distorted structure (for the tetragonal structure it is identical to the bond-length ratio). In both cases, the strain is defined with respect to $a_{p,\text{eq}}$ of bulk LNO; the shift of the zero-strain point in the tetragonal case reflects thus the difference in the lattice constants of the two types of structures. Bottom: Dependence of the octahedral in-plane rotations (γ) and out-of-plane tilts ($\alpha = \beta$) on strain for the fully relaxed distorted structure. Also, structural refinement data from Ref. [46] are shown with diamonds for $\alpha = \beta$ and with circles for γ . Inset: Inclination angle ϕ_m of the pseudocubic axis c_p with respect to the ab plane.

B. Results

The first important effect of strain is the contraction/expansion (for tensile/compressive strain, respectively) of the unit cell in z direction. This is measured by the $c/a \equiv c_p/a_p$ ratio, or equivalently, by the z strain $\epsilon_{zz} \equiv c_p/c_{p,\text{eq}} - 1$, where c_p is the length of the out-of-plane axis of the pseudocubic unit cell.

We display in the top panel of Fig. 1 the results for c/a as a function of strain for both the tetragonal and distorted cases. If one compares the evolution of the c/a ratio for the tetragonal case, in which the dependence is almost perfectly linear, to that of the distorted case, one can see that the octahedra tilts result in a noticeably nonlinear elastic response. At the same time, the ratio of the octahedron bond lengths, l_c/l_a , also displayed in Fig. 1, is very similar in both cases, implying that the internal geometry of the octahedra is similar for the tetragonal and distorted structures. The nonlinear behavior of the c/a ratio in the distorted case reflects thus the evolution of the rotation angles under strain.

Another important structural effect, with direct consequences for the electronic structure, is the different pattern of octahedral rotations found for compressive and tensile strains (the bottom panel of Fig. 1), as previously discussed in Ref. [46]. Octahedral rotations can be characterized by angles α, β, γ of rotations around the x, y axis (out-of-plane rotations) and z axis (in-plane), respectively [39]. In unstrained bulk LaNiO_3 , all three angles are equal $\alpha = \beta = \gamma$, and the system has a rhombohedral symmetry. Under compressive strain, out-of-plane rotations (tilts) are suppressed and at the most negative strain only the in-plane rotation is left, with the structure approaching a higher tetragonal symmetry. The system under tensile strain, on the other hand, prefers octahedra to tilt, with the in-plane rotations being suppressed already at moderate strains. For strains corresponding to LaAlO_3 (LAO) and SrTiO_3 (STO) substrates, the angles are in good agreement with the available experimental data [46], as also shown in Fig. 1. Note, however, that tilt angles in superlattices might differ from those in films [47].

This behavior can be considered as a second-order structural isosymmetric transition that the LNO layer undergoes on crossing over from compressive to tensile strain, whereby the rotation pattern of octahedra changes from $a^0a^0c^-$ (in-plane rotation $\gamma \neq 0, \alpha = \beta \simeq 0$) to $a^-a^-c^0$ (out-of-plane tilting $\alpha = \beta \neq 0, \gamma \simeq 0$).

The rigidity of octahedra dictates that antiphase rotations around three axes in bulk LaNiO_3 must induce distortions of the unit cell, with the pseudocubic vectors a_p, b_p, c_p being inclined with respect to each other [39]. In an epitaxially constrained film, the angles between a_p and b_p are fixed by the substrate and only the c_p axis can relax in such a way as to avoid a strong deformation of the octahedra. This is perfectly illustrated by the dependence of the inclination angle ϕ_m of c_p with respect to the ab plane (inset in Fig. 1). The largest deviation from 90° is taking place around zero strain, which is important for stabilizing the configuration with all angles being equal ($a^-a^-a^-$, as in the bulk). Indeed, when constraining c_p to be orthogonal to the plane, GGA calculations (not shown) yield a very sharp first-order-like transition, with the $a^-a^-a^-$ configuration being unstable at zero strain. This is not consistent with the bulk crystal structure, and emphasizes the importance of letting the structure fully relax in the calculations.

Finally, we would like to mention that earlier works relying on GGA + U calculations predicted that LaNiO_3 films experience bond disproportionation under tensile strain [35,46]. However, these calculations assume some form of magnetic and/or orbital ordering. Recent more precise results obtained within the DFT + DMFT approach indicate that GGA + U overestimates this effect [48], and we therefore do not expect that the bond-disproportionated phase is relevant for the range of strains considered in the present paper. This is also supported by recent experimental results [34].

III. ORBITAL POLARIZATION: EFFECT OF STRUCTURAL DISTORTIONS

In this section, we investigate the effects of structural distortions on the orbital polarization of e_g states in strained

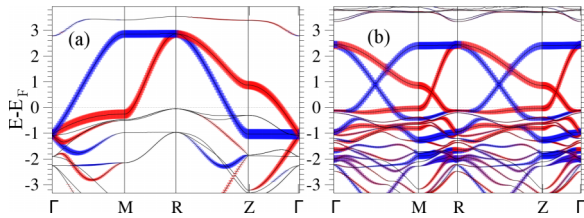


FIG. 2. (Color online) Band structure at zero strain (GGA): (a) tetragonal structure, (b) distorted structure. A fat-band representation is used to indicate orbital character: red (dark) corresponds to d_{z^2} , blue (light) to $d_{x^2-y^2}$ orbitals. A Brillouin zone of the cubic cell is used in all cases. A clear flattening of bands (Γ - M) around the Fermi level is observed for the distorted structure, as a result of hybridization with the t_{2g} states.

LNO. All calculations are performed within GGA: the effects of electronic correlations in the Ni d -shell, and their interplay with structural aspects will be considered in the next section.

We start with a brief review of the basic electronic structure of LNO. The formal valency of Ni ions is 3^+ (d^7), with the ionic ground-state configuration being $t_{2g}^6 e_g^1$. This is only a formal assignment however, since strong covalency and hybridization with oxygen states usually lead to a nominal valency different from the formal one. The GGA band structure of unstrained LNO in both the tetragonal and distorted structures is displayed in Fig. 2. The orbital characters in the local frame of tilted octahedra are obtained by real-space rotation of the basis by tilt angles. The t_{2g} -like bands lie below the Fermi level but are quite close in energy. They are completely filled, and their dispersion is relatively weak at the top of the bands [12]. The behavior of valence electrons is thus almost entirely determined by the e_g states and the oxygen p states hybridized with the e_g states, i.e., the e_g -like bands. In Fig. 2, we also see that in the distorted structure, the bands acquire a more mixed orbital character (away from Γ point) in terms of the orbitals defined in the local reference frame of the (tilted) octahedra. As a result, the relevant bands near the Fermi level have a sizable t_{2g} contribution as well.³

In the presence of epitaxial strain, the changes in the structure induce a lifting of the degeneracy of the e_g states. This is clear from Fig. 3, which displays the GGA band structure under a +3.2% tensile strain. As expected, due to the compression of the octahedra, the center of gravity of the d_{z^2} band is pushed upwards relative to that of the $d_{x^2-y^2}$ band. The bandwidth of the $d_{x^2-y^2}$ band is also reduced (due to the larger in-plane lattice constant). The two bands, however, remain almost completely degenerate at the Γ point due to vanishing d - p hybridization at this point.⁴ Importantly, the described

³Note that the mixing of bands happens only at nonzero k vectors. The orbital characters at Γ point are entirely determined by the local crystal-field symmetry.

⁴Lifting of the degeneracy at the Γ point can be achieved by controlling the direct hoppings (not mediated by oxygens) between Ni d states in plane and perpendicular to the plane [21]. In particular, hoppings are anisotropic in other members of Ruddlesden-Popper series (e.g., A_2BO_4 as in cuprates) or in heterostructures.

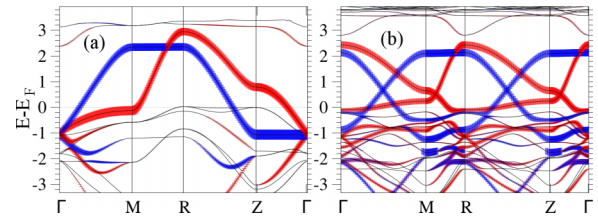


FIG. 3. (Color online) Band structure (GGA) for a +3.2% tensile strain: (a) tetragonal structure, (b) distorted structure. A fat-band representation is used to indicate orbital character: red (dark) corresponds to d_{z^2} , blue (light) to $d_{x^2-y^2}$ orbitals. The center of gravity of the d_{z^2} is pushed upwards, and the bandwidth of the $d_{x^2-y^2}$ band is reduced. Note that the two bands remain degenerate at the Γ point.

properties are still valid even when correlations are taken into account (see Appendix B). The degeneracy lifting of the e_g states can be quantified by defining the intra- e_g crystal-field (CF) splitting as:

$$\Delta_{e_g} \equiv \varepsilon_{z^2} - \varepsilon_{x^2-y^2}, \quad (1)$$

where the level positions ε_{z^2} , $\varepsilon_{x^2-y^2}$ are given by the diagonal terms of the local Hamiltonian (obtained by projecting the Kohn-Sham Hamiltonian onto the e_g states), which is equivalent to finding the center of mass of the projected DOS for each orbital.

This results in a corresponding change in the relative orbital occupancies $n_{x^2-y^2}$, n_{z^2} , leading to OP quantified as

$$P \equiv \frac{n_{x^2-y^2} - n_{z^2}}{n_{x^2-y^2} + n_{z^2}} = \frac{1}{n_{e_g}}(n_{x^2-y^2} - n_{z^2}), \quad (2)$$

which is the quantity of central interest in this paper. An important question is the proper definition of the occupancies $n_{x^2-y^2}, n_{z^2}, n_{e_g} = n_{x^2-y^2} + n_{z^2}$ entering this expression. We now address this question in some detail.

A. Definition of occupancies

Strong d - p hybridization in transition-metal oxides makes orbital occupancies (such as n_{z^2} , $n_{x^2-y^2}$) quite sensitive to the choice of the local basis [31,33] with respect to which these occupancies are calculated. This is particularly pronounced in systems with a small charge-transfer energy, such as nickelates, in which the orbital character of states close to the Fermi level is determined by a mixture of d^7 and $d^8\bar{L}$ states [49–52], each of these states obviously having a different d -electron count.

There are essentially two strategies to define the local-basis Wannier functions differing by the choice of the energy window in which the projection is done, or, equivalently, by the choice of the subset of projected bands. The first way is to choose a broad energy window involving all Ni d -like and oxygen p -like bands (for LaNiO_3 this corresponds to bands within a range $[-8.0, 3.0]$ eV). The resulting localized Wannier (LW) functions $|\chi\rangle_{\text{LW}}$ are well localized, have predominantly d character and yield the total occupation of e_g states close to $n_{e_g} \approx 2$ [20]. On the other hand, choosing a narrow energy window ($[-1.6, 3.0]$ eV) embracing mainly the e_g -like bands around the Fermi level leads to extended Wannier (EW) functions $|\chi\rangle_{\text{EW}}$ with substantial weight on the oxygen sites.

These extended Wannier functions comprise both the localized $\text{Ni}d$ states and a linear combination of the Op states having the same symmetry as the e_g states (p_σ states). The total occupation of e_g states is $n_{e_g} \approx 1$ in this case.

In this paper we will be using the EW-type of basis for the evaluation of the local quantities, including the OP and CF splitting. There are two main reasons justifying this choice, as discussed in more details below: (i) this choice ensures that the calculated OP provides information about the degree of orbital polarization of low-energy quasiparticle bands and (ii) importantly, the OP defined in this manner is consistent with the one measured in XAS and resonant spectroscopy experiments.

Regarding (i), it is natural to define the OP in such a way that a system reaching $P = 100\%$ is associated with a transition from an initially two-sheet (e_g -like) Fermi surface to a single-sheet one ($d_{x^2-y^2}$ -like) when a sufficiently large CF splitting is imposed. In this case, the d_{z^2} band becomes completely unoccupied and the system becomes effectively single-band. The orbital character of these low-energy bands is primarily determined by the symmetry of the local states, the latter being represented by both the $\text{Ni}d$ and Op_σ states. Such states are consistently described by EW-type Wannier functions, $|\chi_{e_g}\rangle_{\text{EW}}$.

From the experimental standpoint (ii), spectroscopic probes such as linear dichroism in XAS and resonant spectroscopies [53] are by design sensitive to the symmetry of the local states. When one wants to extract P from the results of a dichroism measurement, one has to make assumptions about the overlap between the local exciton and both the d states of nickel and the symmetrized oxygen p_σ states. Since the latter penetrate quite deep inside Ni-O octahedra, it is natural to expect a substantial contribution to the OP from the oxygen hole states, which is well captured by the extended EW basis. In other words, we assume that XAS does not promote a core electron to a very localized atomlike Ni state but rather to extended states of mixed $\text{Ni}d$ - Op character.

B. Results and analysis

The top panel of Fig. 4 displays the orbital polarization as a function of strain obtained within GGA. One can see a substantial difference in the behavior of the OP in the tetragonal and distorted structures. In the case of the tetragonal structure, the dependence of P on strain is smooth and lacking any features, as expected from a simple picture where the polarization is induced by a uniform relative shift of the d_{z^2} -like and $d_{x^2-y^2}$ -like bands. In contrast, in the distorted structure the OP is significantly enhanced over the entire range, except for a small region around zero strain where the plot reveals a transitional behavior when going over from compressive to tensile strain. At the same time, the slope of the OP is almost the same at large strains for both types of structure. This implies that the enhancement is due to the electronic structure of the system at small strain.

To understand the cause of the polarization enhancement in the distorted structure as compared to the tetragonal one, we plot the intra- e_g CF splitting, Δ_{e_g} , as a function of strain in the lower panel of Fig. 4. In contrast to the OP, we find

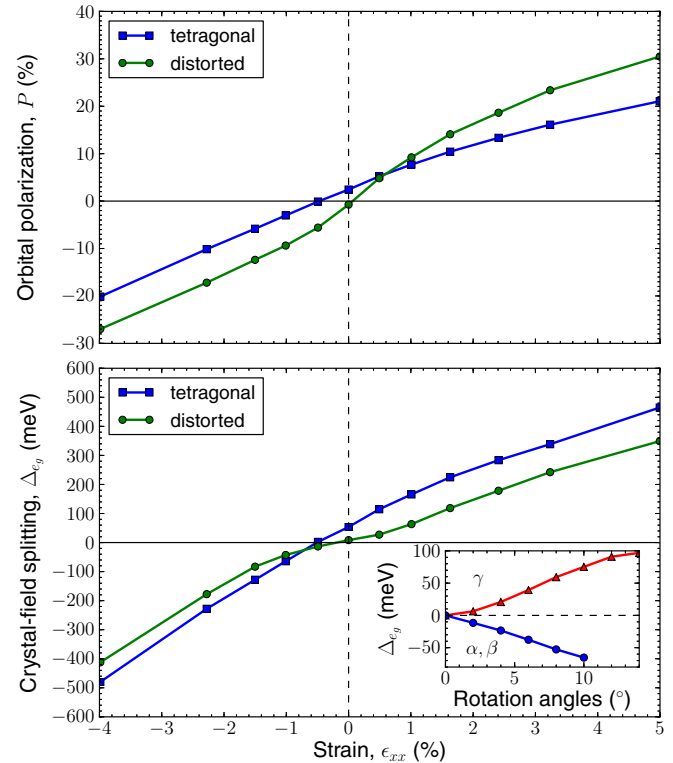


FIG. 4. (Color online) Top: The orbital polarization, P , obtained within GGA as a function of strain for the tetragonal (squares, blue) and distorted structures (circles, green). Bottom: The corresponding e_g crystal-field splitting, Δ_{e_g} , as a function of strain for the tetragonal (squares, blue) and distorted structures (circles, green). Inset: Δ_{e_g} as a function of in-plane and out-of-plane rotation angles (γ and α, β , respectively), with the l_c/l_a ratio fixed to 1.

that the CF splitting is *smaller* in the distorted case. This is expected qualitatively: allowing the structure to relax (mostly by tilting the octahedra) will indeed alleviate the effect of the strain imposed on the structure and reduce the CF splitting.

In order to disentangle the effects of octahedral tilts on Δ_{e_g} from that of the change in bond length ratio l_c/l_a , we have calculated the crystal field as a function of rotation angles γ and α, β , with the ratio l_c/l_a being kept fixed (inset of Fig. 4). Having in mind the dependence of rotation angles on strain [Fig. 1(b)], it is clear that octahedral rotations tend to reduce the absolute value of the crystal-field splitting induced by strain.

Finally, we display in Fig. 5 the OP as a function of CF for each structure. We see that while the tetragonal structure displays an almost perfect linear dependence of P on Δ_{e_g} this dependence has a sharp critical-like behavior for the distorted structure. This reflects the nonlinear feedback of octahedral rotation and tilts when the structure is relaxed.

Defining the orbital polarizability χ_P at small strain from the slope of the dependence of the OP vs CF:

$$P = \chi_P \Delta_{e_g}, \quad (3)$$

we see that χ_P is almost four times larger for the distorted than for the tetragonal structure. In a simple rigid-band model in which the crystal field simply shifts the partial density of states of the d_{z^2} and $d_{x^2-y^2}$ orbitals (denoted by D_z and D_x ,

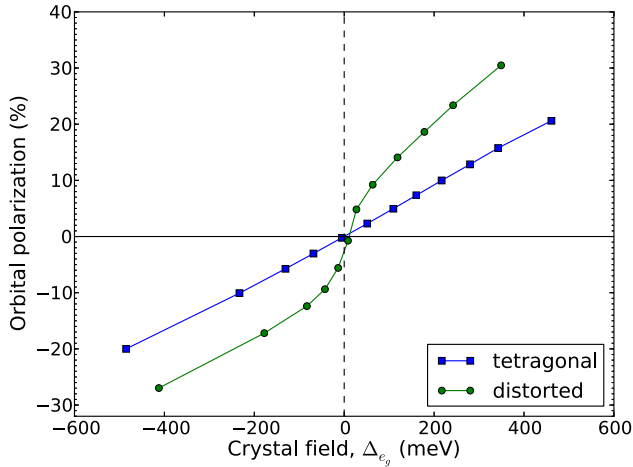


FIG. 5. (Color online) Orbital polarization P obtained within GGA as a function of the crystal-field splitting, Δ_{e_g} , for the tetragonal (squares, blue) and distorted structures (circles, green).

respectively), the orbital susceptibility is easily obtained as:

$$\chi_P = 2 \frac{D_x D_z}{D_x + D_z} = D_{e_g}, \quad (4)$$

in which all density of states are taken at the common Fermi level. The last relation holds when the orbitals are degenerate at zero strain so that $D_x = D_z \equiv D_{e_g}$.

The DOS for the tetragonal and distorted structures are displayed in Figs. 6 and 7, respectively. Remarkably, the Fermi level of the distorted structure falls close to a sharp peak in the DOS, which is not the case for the tetragonal structure for which the Fermi level falls in a featureless flat region. This explains qualitatively the larger orbital susceptibility of the distorted structure. On a quantitative level, the value of χ_P is in rather good agreement with the calculated DOS $D_{e_g} = 0.53 \text{ eV}^{-1}$ and expression (4) for the tetragonal case. In contrast the value of the $D_{e_g} = 0.82 \text{ eV}^{-1}$, 1.6 times larger than for the tetragonal structure, is smaller than the calculated large value of the orbital polarizability enhancement (Fig. 5).

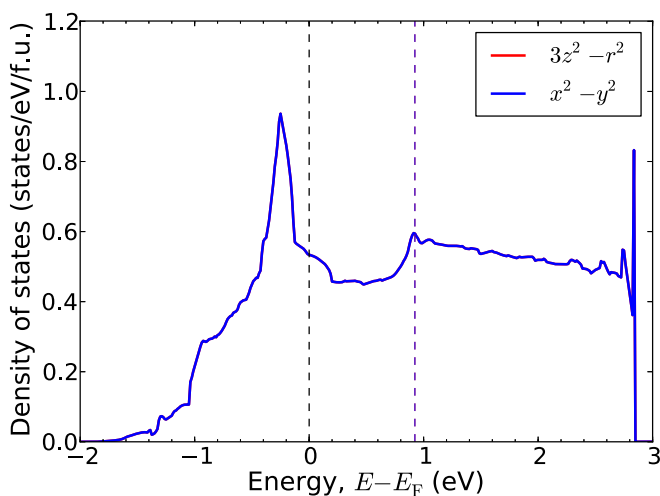


FIG. 6. (Color online) Partial e_g DOS of the tetragonal structure with $c/a = 1$.

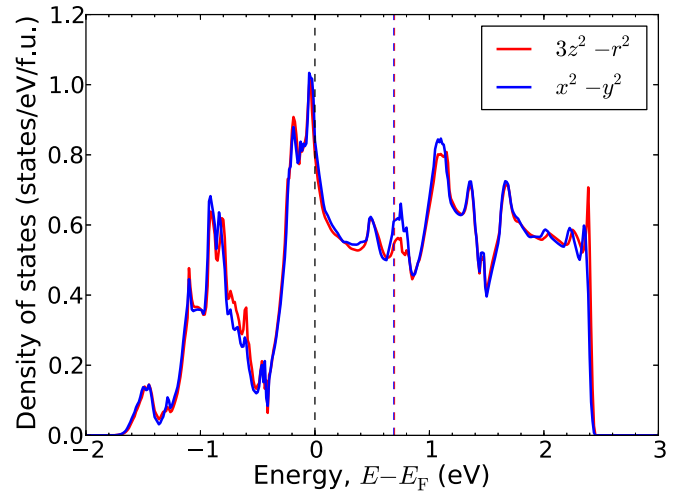


FIG. 7. (Color online) Partial e_g DOS of the distorted structure at zero strain. Keep in mind that this structure is slightly different from the true bulk structure with a higher rhombohedral symmetry.

This is because a rigid-band model does not properly take into account the nonlinearities associated with relaxation and the intrinsic changes in the DOS under strain.

The origin of the peak in the DOS for the distorted structure can be understood by looking at the band structure in Fig. 2. Octahedral tilts lead to hybridization between the e_g states and relatively flat t_{2g} bands. The corresponding flattening of e_g bands near the Fermi level is clearly observed on the projected band structure (Fig. 2). A similar enhancement of the DOS at the Fermi level was reported in earlier works [54].

We have demonstrated that the observed larger orbital polarizability of the distorted structure as compared to the tetragonal structure is due to differences in the electronic structure, and especially due to the hybridization with t_{2g} bands when octahedra relax and tilt. In the next section we consider how the OP is affected by electron correlations.

Finally, it is worth noting that epitaxial strain alone is inefficient in lifting the degeneracy of e_g orbitals at the Γ point [compare, e.g., Figs. 2(a) and 3(a)], which limits its ability to produce very large OP [21,28]. The efficiency can be increased by sandwiching single nickelate layers between insulating layers in a superlattice, confining thus carriers inside the plane and lifting the d_{z^2} band with respect to the $d_{x^2-y^2}$ band [25,29].

IV. ORBITAL POLARIZATION: EFFECT OF CORRELATIONS

We have seen that strain-induced structural distortions lead to rather large values of the orbital polarization in GGA electronic structure calculations. However, as emphasized in the introduction, nickelates are materials with strong electronic correlations. In this section, we investigate how these correlations affect the OP and modify the band-structure values above. Comparison to recent experiments will be made in Sec. V.

A. DFT + DMFT results

We have performed calculations for the relaxed (distorted) structure determined above with a combination of density-functional theory (DFT-GGA) and dynamical mean-field theory (DMFT) [55,56] using the WIEN2TRIQS [57] interface. The DMFT quantum impurity problem has been solved with the numerically exact hybridization-expansion continuous-time quantum Monte Carlo (CT-QMC) method [58] implemented in the TRIQS [57] package. Importantly, localized Wannier (LW) functions are used in defining the many-body Hamiltonian and the corresponding DMFT local impurity problem. These LW functions are defined from $Ni d$ and $O p$ states within a large energy range $[-8.0, 4.0]$ eV. Our GGA + DMFT calculations hence include all relevant oxygen and nickel states, which is physically important in view of the strong hybridization between these states (in contrast to a calculation starting from a low-energy Hamiltonian constructed from an EW basis). Interactions are applied to these local orbitals using a Slater-type parametrization with on-site Coulomb interaction and Hund's coupling $U = 8.0$ eV, $J_H = 1.0$ eV, respectively. The double-counting term is chosen to be of the around-mean-field (AMF) form, in view of the metallic nature of LNO. The calculations were performed only for tensile strains stabilizing the $x^2 - y^2$ orbital (i.e., positive OP, as defined above).

As emphasized above however, the e_g occupancies entering expression (2) must be defined with respect to a basis of extended Wannier functions (EW) as defined in Sec. III A. In order to comply with this physical requirement and to compare in a consistent manner the value of the OP obtained in GGA + DMFT with the band structure GGA results, as well as with experiments, the local Green's function obtained in the GGA + DMFT calculation in the LW basis is thus reprojected onto the EW basis. Details of this procedure are provided in Appendix A.

The resulting orbital polarization as a function of strain is presented in Fig. 8 along with corresponding GGA values. For all values of tensile strain we observe that correlations

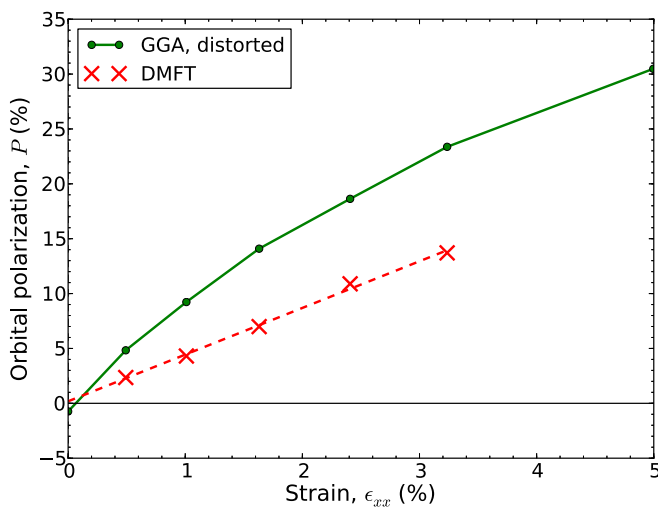


FIG. 8. (Color online) OP as a function of strain obtained within GGA (green solid line) and within GGA + DMFT (red crosses; dashed line is a linear fit) for the distorted structure.

tend to reduce the OP as compared to the GGA values. This finding is in agreement with previous calculations of LNO-based heterostructures using DMFT with a similar choice of the localized Wannier basis [23], although quantitative comparison is difficult in view of the difference in the systems studied. As noted in the introduction, DMFT calculations performed using the very different framework of a low-energy description involving only e_g states (defined, e.g., from an EW basis) found a large enhancement of the OP by correlation effects [21,22]. This raises the important question of what is the appropriate minimal low-energy model for nickelates [29], a question that is beyond the scope of the present paper but which we intend to return to in future work.

B. Hund's rule coupling and the reduction of orbital polarization

We now provide a physical discussion of the correlation-induced mechanisms that tend to suppress orbital polarization.

As emphasized in model studies (see, e.g., Ref. [32]), the on-site repulsion U has a tendency to *increase* the OP. This is because the crystal-field splitting should be compared to the electronic kinetic energy, which is reduced when U (and hence the quasiparticle bandwidth) is increased. Hence, the orbital polarizability, proportional to the inverse of the kinetic energy, is increased by this effect.

In contrast, the Hund's rule coupling competes with the crystal-field splitting and tends to reduce the OP, as also emphasized in previous studies (for a review, see, e.g., Ref. [59]). These opposite effects of U and J_H are clearly illustrated by Fig. 9, in which we display the results of GGA + DMFT calculations performed at several values of the Hund's coupling, for LNO subject to the largest tensile strain

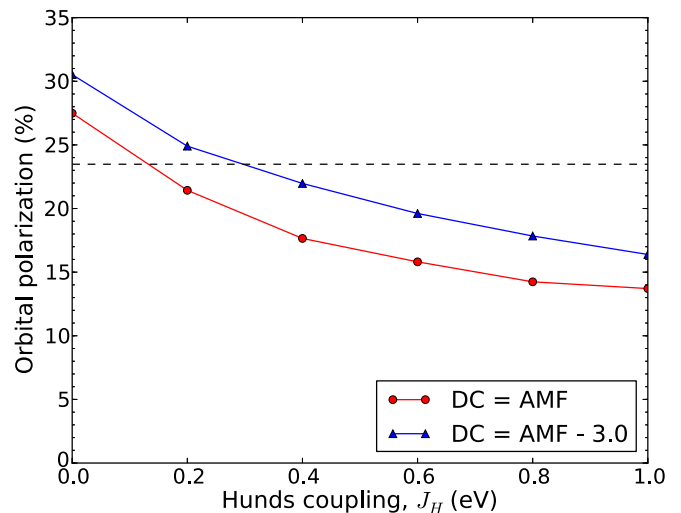


FIG. 9. (Color online) Orbital polarization as a function of Hund's rule coupling J_H for $U = 8.0$ eV, obtained within GGA + DMFT for LNO with tensile strain $\epsilon_{xx} = 3.24\%$. The dashed horizontal line indicates the GGA value. The results are displayed for two values of the double counting: the around mean-field (AMF) one and one in which the double-counting potential is shifted by -3 eV from the AMF value (the shift of the double counting can be viewed as a static contribution of U_{pd} within Hartree-Fock approximation).

considered in this work. For small J_H , the OP is enhanced by correlations as compared to the GGA value, while increasing J_H quickly brings the OP down to values smaller than the GGA ones.

We now discuss qualitatively the physical origin of this effect of the Hund's coupling, starting from the atomic limit. The ground-state configuration of Ni ions can be described as a mixture of d^7 and $d^8\bar{L}$ configurations (see Sec. III A) [49–51]. In a $d^8\bar{L}$ configuration with two d electrons in the two e_g orbitals, the OP will be suppressed because the CF splitting has to compete with the rather large Hund's coupling $J_H \sim 1$ eV, which tends to put the two electrons in different orbitals in a high-spin $S = 1$ state. The orbital polarizability is obviously zero in such a state. The relevance of the $d^8\bar{L}$ configuration in explaining the observed reduction of the OP by the Hund's rule coupling has been emphasized in Ref. [23].

Nevertheless, this should not be taken as evidence that the $d^8\bar{L}$ configuration dominates the wave function of Ni ions. Indeed, as we now explain, the Hund's rule coupling also acts to reduce the OP for the d^7 component of the wave function. At first sight, this statement appears surprising: obviously, the competition of Hund's rule coupling and CF splitting is absent in the atomic limit of individual atoms, since the d^7 configuration corresponds to a completely filled t_{2g} shell and one electron in the doubly degenerate e_g shell. For an isolated atom in this configuration, a small crystal field can fully polarize the orbital configuration irrespective of J_H .

However, this no longer applies when intersite hopping is taken into account. In order to illustrate this point, we consider a simple two-site model (Fig. 10). Each site carries two orbitals (i.e., we do not consider the filled t_{2g} orbitals), a hopping t connects only orbitals of the same type from one site to another, and there is one electron per site on average (d^7 configuration,

corresponding to one electron in the e_g shell). The levels on each site are split by a CF Δ_{CF} . There are $4^2 = 16$ states in the low-energy Hilbert space with no double occupancy. A given eigenstate in this low-energy subspace is characterized by the total spin $S = 0, 1$ and the total orbital pseudospin $T = 0, 1$ (with $T = 0$ corresponding to an orbitally degenerate state and $T = 1$ to an orbitally polarized one).

In the limit $t \ll U$ the low-energy dynamics is determined by three types of superexchange processes shown in Fig. 10(a), with the parameters

$$\begin{aligned} (S = 1, T = 1): & \text{ no hopping is allowed,} \\ \text{spin } (S = 0, T = 1): & J_s = \frac{4t^2}{U}, \\ \text{orbital } (S = 1, T = 0): & J_o = \frac{4t^2}{U - 3J_H}, \\ \text{mixed } (S = 0, T = 0): & J_m = \frac{4t^2}{U - 2J_H}. \end{aligned}$$

The superexchange splits the original 16 configurations into four groups of degenerate states corresponding to four possible combinations of total spin and pseudospin moments [see Fig. 10(b)]. Choosing the energy of the $(S = 1, T = 1)$ configuration as zero and evaluating the energies of the three other configurations, one readily obtains that depending on the value of Δ_{CF} the ground-state configuration will be one of the two following ones:

$$\begin{aligned} S = 0, T = 1 & \quad \text{with energy } E = -J_s, \\ S = 1, T = 0 & \quad \text{with energy } E = \Delta_{CF} - J_o. \end{aligned}$$

Hence, we conclude that for small CF $\Delta_{CF} < J_o - J_s$ (i.e., for $\Delta_{CF} < 12t^2 J_H / U^2$ to first order in J_H / U), the orbitally degenerate configuration $(S = 1, T = 0)$ is the ground state, while orbital polarization takes over above this critical value. Hence, increasing J_H does increase the stability of the orbitally degenerate (unpolarized) state due to the effect of intersite spin and orbital superexchange. As a side remark, we mention that even though DMFT considers a single-site effective problem, it does capture these intersite effects in the response of the system to a *uniform* field (coupling either to orbitals or spin degrees of freedom), as explained in Ref. [32].

This analysis of course applies to the strong-coupling localized limit of small hopping, and should not be applied quantitatively to LNO, which is a metal. However, it does make the point that Hund's coupling acts to reduce the OP even when the nominal atomic configuration is d^7 . At weak coupling, a perturbative analysis leads to similar qualitative conclusions: the orbital polarizability is enhanced by correlations, as compared to the free-electron one, when $J_H < U/5$, while it is suppressed for $J_H > U/5$ (see Ref. [59]).

We conclude that the Hund's coupling-induced suppression of the orbital polarization actually applies to both the $d^8\bar{L}$ and d^7 configurations. In the latter case, the suppression is mediated by intersite fluctuations involving virtual d^8 states. This suppression should not thus be taken as evidence that $d^8\bar{L}$ is the dominant component of the wave function in LNO (although it certainly has a sizable weight, in view of the strong hybridization with oxygen states). Finally, we note that

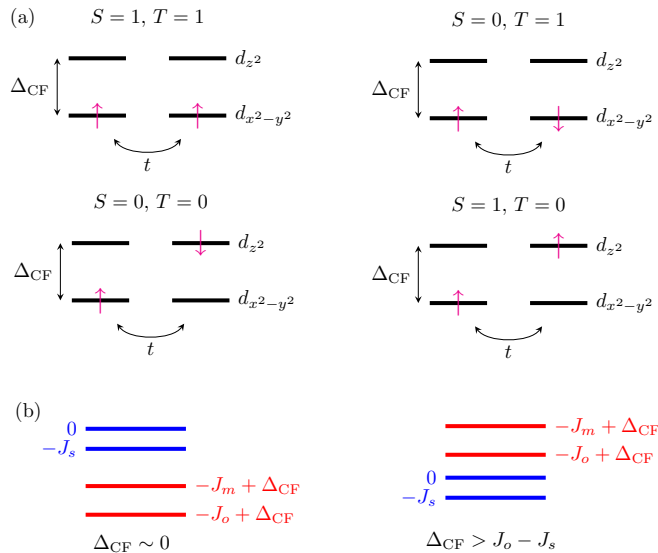


FIG. 10. (Color online) (a) Four types of configurations of the two-site model corresponding to four combinations of quantum numbers S and T . (b) Many-body low-energy spectrum produced by the superexchange processes for small CF splitting (left) and for large CF splitting (right).

the analysis of the simple two-site model above shows that the Hund's coupling tends to promote an intersite ferromagnetic alignment of spins in the orbitally compensated state with $T = 0$, due to the intersite orbital superexchange. Indeed, the magnetic susceptibility of LNO displays a large Stoner enhancement in LaNiO_3 [9,10,60].

V. COMPARISON TO SPECTROSCOPY EXPERIMENTS

In this section, we compare our DFT + DMFT results for the orbital polarization as a function of strain to the recent experimental results of Wu *et al.* [34]. In these experiments, both dichroism measurements in XAS and resonant reflectometry were performed on $(\text{LNO})_4/(\text{RMO})_4$ heterostructures, for various substrates RMO_3 (corresponding to different imposed strains). With the aid of sum rules the ratio of hole occupancies of e_g states, $X = h_{z^2}/h_{x^2-y^2}$, was extracted. This ratio can be converted into the OP as defined in Eq. (2) by the relation

$$P = \left(\frac{4}{n_{e_g}} - 1 \right) \frac{X - 1}{X + 1}. \quad (5)$$

This expression involves the total occupancy in the e_g states, a quantity that is not directly accessible to these experiments. In Ref. [34] a value $n_{e_g} = 1$ corresponding to low-energy Wannier construction (EW basis) was used with a goal to compare the values of P with the theoretical values obtained by integrating the DOS of low-energy antibonding states [23]. The XAS measurements yield a value of the OP, P_{av} , averaged over four layers of LNO in the heterostructure. To disentangle interfacial and strain effects, additional measurements using q -resolved resonant reflectivity were performed, which allowed the experimentalists to obtain the OP for individual layers: two B layers adjacent to the interface with RMO and two inner A layers in between the B layers, with corresponding OPs P_A and P_B that average to P_{av} .

The experimental results along with the calculated OP already presented in the previous section are shown together in Fig. 11. As the geometry employed in our calculations takes into account only a uniform biaxial strain and assumes no interfacial effects, the numerical results should be compared to the A -layer data (P_A), which are less influenced by the interface. With this in mind, one can see that pure GGA values substantially overestimate the polarization and that the agreement between our GGA + DMFT results and experimental values is fairly good.

This comparison between our theoretical results and experiments can actually be further refined by noting that the interpretation of both the hole h_{e_g} and the total e_g occupancies is basis dependent, as has already been discussed in Sec. III A. The ambiguity about n_{e_g} can be resolved by simply using the value of X , as originally introduced in Ref. [34], rather than P when comparing calculations with experiment. This is done in Fig. 12 where we show theoretical values of X and experimental layer-resolved values, X_A . Interestingly, there is a noticeable improvement in the agreement between our theoretical results and experimental values when the comparison is done in this manner.

The difference between these two analyses of P and X can be traced back to the deviation of the actual e_g occupancy as calculated in GGA + DMFT from the nominal

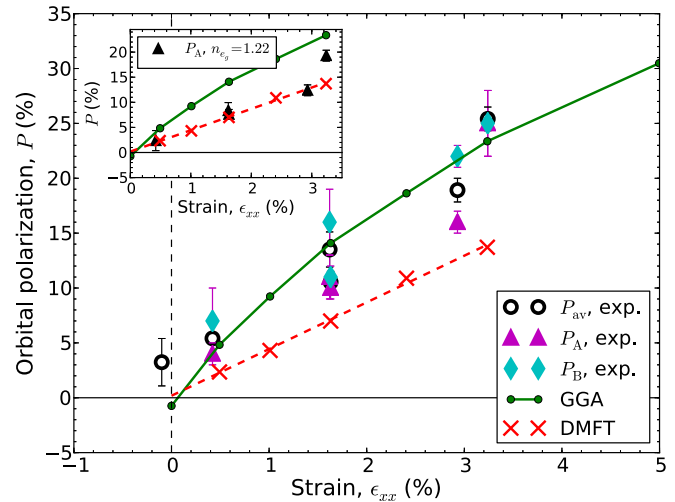


FIG. 11. (Color online) The orbital polarization, P , as a function of strain for the distorted structure (circles, green), GGA + DMFT (red crosses), and experiment, with diamonds, triangles and open circles corresponding respectively to P_B , P_A , and P_{av} obtained from XLD in Ref. [34]. Inset: Reinterpretation of the experimental data with a theoretical value of $n_{e_g} = 1.22$.

value $n_{e_g} = 1$ assumed in the analysis of the experimental data in Ref. [34]. Indeed, if we take the GGA + DMFT value $n_{e_g} \approx 1.22$ (practically independent of strain) and reinterpret the experiments by recalculating the electron OP from the measured value of X_A (inset of Fig. 11), we get a noticeable shift of the data and a correspondingly improved agreement for P . This reflects the improved agreement obtained when comparing directly the measured hole-occupancy ratio X .

To summarize, the approach of comparing hole-occupancy ratio, X [or, equivalently, hole orbital polarization $(X - 1)/(X + 1)$] directly with experiment has a two-fold advantage. On one hand, one avoids relying on the value of n_{e_g} —a quantity poorly defined from the experimental point of view. On the other hand, the energy scale of hole occupancies of d or mixed d - p states is uniquely fixed by the extent of unoccupied

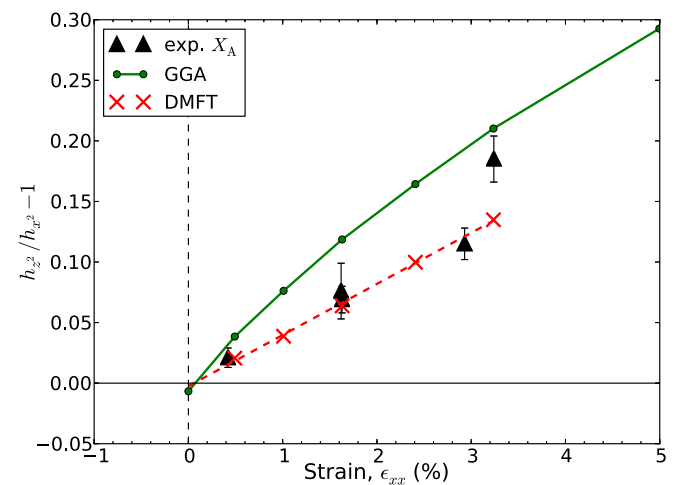


FIG. 12. (Color online) The ratio of the hole occupancies, X , as a function of strain (for experimental points the value for the inner layers, X_A , is used).

(antibonding) states above the Fermi level, which makes the hole OP independent of the choice of the integration limits taken when evaluating the occupancies.

Also, we note that the hole-occupancy ratio X is less sensitive to the choice of projectors (localized or extended Wannier) used in the evaluation of occupancies. Within DFT, the low-energy Op_σ states have the same symmetry and almost the same positions as corresponding Ni e_g states, which makes their noninteracting DOS very similar in shape. The ratio of hole occupancies evaluated within DFT is thus practically independent of the type of projectors used. In DMFT calculations within LW basis, correlations mostly affect d states, shifting their positions and renormalizing the CF splitting. However, even in this case the difference between X_{EW} and X_{LW} does not exceed 50% of X_{EW} .

VI. CONCLUSION

We have investigated the effect of structural distortions and relaxation, as well as the effect of electronic correlations on the orbital polarization of LaNiO_3 epitaxial films.

From the structural point of view, we have emphasized the interplay between distortions and relaxation in this material. Under tensile strain, in-plane rotations are suppressed and out of plane tilts are favored [46]. Surprisingly, this leads to a larger orbital polarization than for a tetragonally constrained structure subject to the same strain, even though the intra- e_g crystal-field splitting is comparatively smaller for the relaxed distorted structure. We have shown that this effect is due to the mixing of e_g states with low-dispersion t_{2g} states in the distorted structure.

This effect by itself would lead to rather large values of the OP, larger than those reported in the recent experiment of Wu *et al.* [34]. Electron correlations lead to a reduction of the OP however, due to the effect of the Hund's rule coupling, as previously emphasized by Han *et al.* [23]. This suppression is often interpreted as a signature of the dominance of the $d^8\bar{L}$ configuration in the ground state: in this configuration the CF splitting has to overcome the Hund's exchange J_H to induce an OP and a concomitant high-spin to low-spin transition. However, we point out that the Hund's exchange also competes with the CF for the d^7 configuration because the strength of the intersite orbital superexchange depends on the Hund's coupling.

Our theoretical results for the orbital polarization as a function of strain are in good agreement with the experimental values reported by Wu *et al.* [34]. We have also emphasized that a more direct comparison to linear dichroism XAS experiments (and better agreement with the experimental data) is achieved when directly comparing the ratio of hole occupancies.

The presented results suggest that although the OP in LaNiO_3 can be efficiently controlled by crystal-structure design, achieving a higher degree of orbital polarization is hampered by the three following effects.

(i) Degeneracy of the two e_g bands at the Γ point in LaNiO_3 strained film geometry due to vanishing d - p hybridization and practically isotropic direct hoppings in plane and out of plane typical of an ABO_3 perovskite structure. This problem can be circumvented either by choosing a less symmetric bulk structure (such as an A_2BO_4 -type structure) or by

engineering heterostructures with a single layer of LNO sandwiched between insulating layers [19,25,28,29]; however, such structures are generally difficult to fabricate.

(ii) Small charge-transfer energy (possible even negative [31]), resulting in a significant contribution of the $d^8\bar{L}$ configuration.

(iii) The reduction of the OP by the Hund's rule coupling.

Further progress in the field aiming at achieving larger or even full orbital polarization [19,21,22] will have to overcome these effects by considering appropriate materials and heterostructures.

ACKNOWLEDGMENTS

We are grateful to Sara Catalano, Stefano Gariglio, Marta Gibert, Jean-Marc Triscone, and all other members of the Triscone group in Geneva, as well as to Philipp Hansmann, Andrew J. Millis, Leonid Pourovskii, Dirk van der Marel, George Sawatzky, and Michel Viret, for many useful discussions. We are indebted to Eva Benckiser, Meng Wu, and Bernhard Keimer for discussions about their data and for making them available to us. Support for this work was provided by the Swiss National Science Foundation (Grant No. 20021-146586) and MaNEP, by a grant from the European Research Council (ERC-319286 QMAC), and by the Swiss National Supercomputing Centre (CSCS) under Project ID s404.

APPENDIX A

Here we outline the routine of reprojecting the impurity Green's function (GF) to get occupation numbers from DMFT calculations that are consistent with those obtained previously in pure GGA calculations. The local impurity problem in the DMFT self-consistency cycle is constructed using projectors $P_{mv}^{\text{LW}}(\mathbf{k})$ defined within energy window $[-8.0, 4.0]$ eV (as described in Sec. IV A), which defines the resulting (converged) impurity GF as

$$G_{mm'}^{\text{loc,LW}}(i\omega_n) = \sum_{\mathbf{k}v v'} P_{mv}^{\text{LW}}(\mathbf{k}) G_{vv'}^{\text{band}}(\mathbf{k}, i\omega_n) [P_{v'm'}^{\text{LW}}]^*(\mathbf{k}),$$

$$G_{vv'}^{\text{band}}(\mathbf{k}, i\omega_n) = \left([i\omega_n + \mu - \varepsilon_{\mathbf{k}v}] \delta_{v,v'} - \sum_{mm'} [P_{vm}^{\text{LW}}]^*(\mathbf{k}) \Sigma_{mm'}^{\text{loc}}(i\omega_n) P_{m'v'}^{\text{LW}}(\mathbf{k}) \right)^{-1},$$

where $\Sigma_{mm'}^{\text{loc}}(i\omega_n)$ is the converged self-energy and indices m run over all five d orbitals.

The occupation numbers and the OP obtained directly from this impurity GF will be inconsistent with the OP given in Sec. III as $\sum_{mm'}^{\text{loc}} \rightarrow 0$ because of the difference in the basis sets. To get consistent occupation numbers, n_l , with index $l = 1, 2$ running only over e_g orbitals, we project the above band GF, $G_{vv'}^{\text{band}}(\mathbf{k}, i\omega_n)$ using the EW basis (energy window

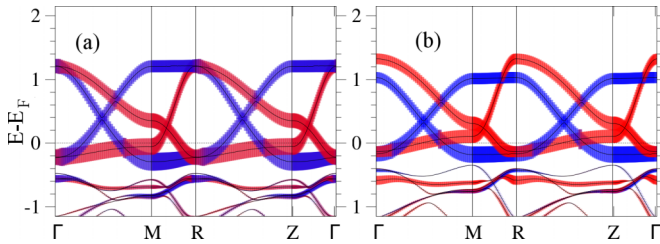


FIG. 13. (Color online) Renormalized band structure of quasiparticles obtained using GGA + DMFT (distorted structure): (a) 0.0% strain (b) +3.2% strain. The figures are to be compared with Figs. 2 and 3 (note that the scale of the ordinate is different here).

$[-1.6, 4.0]$ eV projectors, $P_{lv}^{\text{EW}}(\mathbf{k})$,

$$n_l = \frac{1}{\beta} \sum_{i\omega_n} G_{ll}^{\text{loc,EW}}(i\omega_n) e^{i\omega_n 0^+},$$

$$G_{ll'}^{\text{loc,EW}}(i\omega_n) = \sum_{\mathbf{k}v'v''} P_{lv}^{\text{EW}}(\mathbf{k}) G_{v'v''}^{\text{band}}(\mathbf{k}, i\omega_n) [P_{v'l'}^{\text{EW}}]^*(\mathbf{k}).$$

APPENDIX B

To demonstrate the effect of correlations on the band structure we present the quasiparticle band structure resulting from GGA + DMFT calculations for two cases: unstrained [Fig. 13(a)] and for tensile strain [Fig. 13(b)]. Apart from an overall narrowing of the bands in both cases, one can see a significant lifting of the e_g states at the Γ point. There is also a change in the Fermi surface topology visible along the $\Gamma - M$ line, which is in accord with recent results from angular-resolved photoemission spectroscopy [61]. In the experimental work, the appearance of the hole pocket at the M point was attributed to correlation effects in a sample under tensile strain. The pockets, however, appear already in GGA calculations if one considers a fully relaxed distorted structure, as can be seen from comparing the band structures for tetragonal and distorted cases in Figs. 2 and 3.

- [1] D. G. Schlom, L.-Q. Chen, C.-B. Eom, K. M. Rabe, S. K. Streiffer, and J.-M. Triscone, *Annu. Rev. Mater. Res.* **37**, 589 (2007).
- [2] P. Zubko, S. Gariglio, M. Gabay, P. Ghosez, and J.-M. Triscone, *Annu. Rev. Condens. Matter Phys.* **2**, 141 (2011).
- [3] J. M. Rondinelli and N. A. Spaldin, *Adv. Mater.* **23**, 3363 (2011).
- [4] H. Y. Hwang, Y. Iwasa, M. Kawasaki, B. Keimer, N. Nagaosa, and Y. Tokura, *Nat. Mater.* **11**, 103 (2012).
- [5] M. Gibert, P. Zubko, R. Scherwitzl, J. Iniguez, and J.-M. Triscone, *Nat. Mater.* **11**, 195 (2012).
- [6] A. V. Boris, Y. Matiks, E. Benckiser, A. Frano, P. Popovich, V. Hinkov, P. Wochner, M. Castro-Colin, E. Detemple, V. K. Malik, C. Bernhard, T. Prokscha, A. Suter, Z. Salman, E. Morenzoni, G. Cristiani, H.-U. Habermeier, and B. Keimer, *Science* **332**, 937 (2011).
- [7] M. L. Medarde, *J. Phys.: Condens. Matter* **9**, 1679 (1997).
- [8] G. Catalan, *Phase Transit.* **81**, 729 (2008).
- [9] K. Sreedhar, J. M. Honig, M. Darwin, M. McElfresh, P. M. Shand, J. Xu, B. C. Crooker, and J. Spalek, *Phys. Rev. B* **46**, 6382 (1992).
- [10] X. Q. Xu, J. L. Peng, Z. Y. Li, H. L. Ju, and R. L. Greene, *Phys. Rev. B* **48**, 1112 (1993).
- [11] K. Rajeev, G. Shivashankar, and A. Raychaudhuri, *Solid State Comm.* **79**, 591 (1991).
- [12] R. Eguchi, A. Chainani, M. Taguchi, M. Matsunami, Y. Ishida, K. Horiba, Y. Senba, H. Ohashi, and S. Shin, *Phys. Rev. B* **79**, 115122 (2009).
- [13] D. G. Ouellette, S. B. Lee, J. Son, S. Stemmer, L. Balents, A. J. Millis, and S. J. Allen, *Phys. Rev. B* **82**, 165112 (2010).
- [14] A. X. Gray, A. Janotti, J. Son, J. M. LeBeau, S. Ueda, Y. Yamashita, K. Kobayashi, A. M. Kaiser, R. Sutarto, H. Wadati, G. A. Sawatzky, C. G. Van de Walle, S. Stemmer, and C. S. Fadley, *Phys. Rev. B* **84**, 075104 (2011).
- [15] R. Scherwitzl, P. Zubko, C. Lichtensteiger, and J.-M. Triscone, *Appl. Phys. Lett.* **95**, 222114 (2009).
- [16] J. Son, P. Moetakef, J. M. LeBeau, D. Ouellette, L. Balents, S. J. Allen, and S. Stemmer, *Appl. Phys. Lett.* **96**, 062114 (2010).
- [17] R. Scherwitzl, S. Gariglio, M. Gabay, P. Zubko, M. Gibert, and J.-M. Triscone, *Phys. Rev. Lett.* **106**, 246403 (2011).
- [18] A. Frano, E. Schierle, M. W. Haverkort, Y. Lu, M. Wu, S. Blanco-Canosa, U. Nwankwo, A. V. Boris, P. Wochner, G. Cristiani, H. U. Habermeier, G. Logvenov, V. Hinkov, E. Benckiser, E. Weschke, and B. Keimer, *Phys. Rev. Lett.* **111**, 106804 (2013).
- [19] J. Chaloupka and G. Khaliullin, *Phys. Rev. Lett.* **100**, 016404 (2008).
- [20] X. Deng, M. Ferrero, J. Mravlje, M. Aichhorn, and A. Georges, *Phys. Rev. B* **85**, 125137 (2012).
- [21] P. Hansmann, X. Yang, A. Toschi, G. Khaliullin, O. K. Andersen, and K. Held, *Phys. Rev. Lett.* **103**, 016401 (2009).
- [22] P. Hansmann, A. Toschi, X. Yang, O. K. Andersen, and K. Held, *Phys. Rev. B* **82**, 235123 (2010).
- [23] M. J. Han, X. Wang, C. A. Marianetti, and A. J. Millis, *Phys. Rev. Lett.* **107**, 206804 (2011).
- [24] H. Chen, D. P. Kumah, A. S. Disa, F. J. Walker, C. H. Ahn, and S. Ismail-Beigi, *Phys. Rev. Lett.* **110**, 186402 (2013).
- [25] H. Chen, A. J. Millis, and C. A. Marianetti, *Phys. Rev. Lett.* **111**, 116403 (2013).
- [26] A. Rüegg, C. Mitra, A. A. Demkov, and G. A. Fiete, *Phys. Rev. B* **88**, 115146 (2013).
- [27] D. Doennig, W. E. Pickett, and R. Pentcheva, *Phys. Rev. B* **89**, 121110 (2014).
- [28] X. Yang and O. K. Andersen, Annual Report of the Max-Planck Institute for Solid State Research, 74 (2010).
- [29] M. J. Han, C. A. Marianetti, and A. J. Millis, *Phys. Rev. B* **82**, 134408 (2010).
- [30] V. I. Anisimov, D. Bukhvalov, and T. M. Rice, *Phys. Rev. B* **59**, 7901 (1999).
- [31] T. Mizokawa, D. I. Khomskii, and G. A. Sawatzky, *Phys. Rev. B* **61**, 11263 (2000).
- [32] A. I. Poteryaev, M. Ferrero, A. Georges, and O. Parcollet, *Phys. Rev. B* **78**, 045115 (2008).
- [33] N. Parragh, G. Sangiovanni, P. Hansmann, S. Hummel, K. Held, and A. Toschi, *Phys. Rev. B* **88**, 195116 (2013).

- [34] M. Wu, E. Benckiser, M. W. Haverkort, A. Frano, Y. Lu, U. Nwankwo, S. Brück, P. Audehm, E. Goering, S. Macke, V. Hinkov, P. Wochner, G. Christiani, S. Heinze, G. Logvenov, H.-U. Habermeier, and B. Keimer, *Phys. Rev. B* **88**, 125124 (2013).
- [35] J. Chakhalian, J. M. Rondinelli, J. Liu, B. A. Gray, M. Kareev, E. J. Moon, N. Prasai, J. L. Cohn, M. Varela, I. C. Tung, M. J. Bedzyk, S. G. Altendorf, F. Strigari, B. Dabrowski, L. H. Tjeng, P. J. Ryan, and J. W. Freeland, *Phys. Rev. Lett.* **107**, 116805 (2011).
- [36] A. Blanca-Romero and R. Pentcheva, *Phys. Rev. B* **84**, 195450 (2011).
- [37] J. B. Torrance, P. Lacorre, A. I. Nazzal, E. J. Ansaldo, and C. Niedermayer, *Phys. Rev. B* **45**, 8209 (1992).
- [38] J. L. García-Muñoz, J. Rodríguez-Carvajal, P. Lacorre, and J. B. Torrance, *Phys. Rev. B* **46**, 4414 (1992).
- [39] A. M. Glazer, *Acta Cryst. B* **28**, 3384 (1972).
- [40] A. M. Glazer, *Acta Cryst. A* **31**, 756 (1975).
- [41] J. P. Perdew, K. Burke, and M. Ernzerhof, *Phys. Rev. Lett.* **77**, 3865 (1996).
- [42] P. E. Blöchl, *Phys. Rev. B* **50**, 17953 (1994).
- [43] G. Kresse and D. Joubert, *Phys. Rev. B* **59**, 1758 (1999).
- [44] G. Kresse and J. Hafner, *Phys. Rev. B* **47**, 558 (1993).
- [45] G. Kresse and J. Furthmüller, *Phys. Rev. B* **54**, 11169 (1996).
- [46] S. J. May, J.-W. Kim, J. M. Rondinelli, E. Karapetrova, N. A. Spaldin, A. Bhattacharya, and P. J. Ryan, *Phys. Rev. B* **82**, 014110 (2010).
- [47] J. Hwang, J. Son, J. Y. Zhang, A. Janotti, C. G. Van de Walle, and S. Stemmer, *Phys. Rev. B* **87**, 060101 (2013).
- [48] H. Park, A. J. Millis, and C. A. Marianetti, *Phys. Rev. B* **89**, 245133 (2014).
- [49] M. Abbate, G. Zampieri, F. Prado, A. Caneiro, J. M. Gonzalez-Calbet, and M. Vallet-Regi, *Phys. Rev. B* **65**, 155101 (2002).
- [50] J. Liu, S. Okamoto, M. van Veenendaal, M. Kareev, B. Gray, P. Ryan, J. W. Freeland, and J. Chakhalian, *Phys. Rev. B* **83**, 161102 (2011).
- [51] T. Mizokawa, A. Fujimori, H. Namatame, K. Akeyama, and N. Kosugi, *Phys. Rev. B* **49**, 7193 (1994).
- [52] E. J. Moon, J. M. Rondinelli, N. Prasai, B. A. Gray, M. Kareev, J. Chakhalian, and J. L. Cohn, *Phys. Rev. B* **85**, 121106 (2012).
- [53] E. Benckiser, M. W. Haverkort, S. Brück, E. Goering, S. Macke, A. Frañó, X. Yang, O. K. Andersen, G. Christiani, H.-u. Habermeier, A. V. Boris, I. Zegkinoglou, P. Wochner, H.-j. Kim, V. Hinkov, and B. Keimer, *Nat. Mater.* **10**, 189 (2011).
- [54] N. Hamada, *J. Phys. Chem. Solids* **54**, 1157 (1993).
- [55] M. Aichhorn, L. Pourovskii, V. Vildosola, M. Ferrero, O. Parcollet, T. Miyake, A. Georges, and S. Biermann, *Phys. Rev. B* **80**, 085101 (2009).
- [56] M. Aichhorn, L. Pourovskii, and A. Georges, *Phys. Rev. B* **84**, 054529 (2011).
- [57] M. Ferrero and O. Parcollet, TRIQS: a Toolbox for Research on Interacting Quantum Systems, <http://ipht.cea.fr/triqs>
- [58] E. Gull, A. J. Millis, A. I. Lichtenstein, A. N. Rubtsov, M. Troyer, and P. Werner, *Rev. Mod. Phys.* **83**, 349 (2011).
- [59] A. Georges, L. D. Medici, and J. Mravlje, *Annu. Rev. Condens. Matter Phys.* **4**, 137 (2013).
- [60] J.-S. Zhou, J. B. Goodenough, B. Dabrowski, P. W. Klamut, and Z. Bukowski, *Phys. Rev. Lett.* **84**, 526 (2000).
- [61] H. K. Yoo, S. Ill Hyun, L. Moreschini, H.-D. Kim, Y. J. Chang, C. H. Sohn, D. W. Jeong, S. Sinn, Y. S. Kim, A. Bostwick, E. Rotenberg, J. H. Shim, and T. W. Noh, [arXiv:1406.2433](https://arxiv.org/abs/1406.2433) [cond-mat.str-el].